Article ID: 1006-8775(2023) 02-0191-13

Future Changes in the Relationship Between the South and East Asian Summer Monsoons in CMIP6 Models

CHEN Hong-jing (陈虹静)[1], Song YANG (杨 崧)[1, 2, 3], WEI Wei (魏 维)[1, 2, 3]
(1. School of Atmospheric Sciences, Sun Yat-sen University, Zhuhai, Guangdong 519082 China;
2. Southern Marine Science and Engineering Guangdong Laboratory (Zhuhai), Zhuhai, Guangdong 519000 China;
3. Guangdong Province Key Laboratory for Climate Change and Natural Disaster Studies,
Sun Yat-sen University, Zhuhai, Guangdong 519082 China)

Abstract: The future changes in the relationship between the South Asian summer monsoon (SASM) and the East Asian summer monsoon (EASM) are investigated by using the high-emissions Shared Socioeconomic Pathway 5-8.5 (SSP5-8.5) experiments from 26 coupled models that participated in the phase 6 of the Coupled Model Intercomparison Project (CMIP6). Six models, selected based on their best performance in simulating the upper- and lower-level pathways related to the SASM-EASM teleconnection in the historical run, can capture the positive relationship between the SASM and the rainfall over northern China. In the future scenario, the upper-level teleconnection wave pattern connecting the SASM and the EASM exhibits a significant weakening trend, due to the rainfall anomalies decrease over the northern Indian Peninsula in the future. At the lower level, the western North Pacific anticyclone is projected to strengthen in the warming climate. The positive (negative) rainfall anomalies associated with positive (negative) SASM rainfall anomalies are anticipated to extend southward from northern China to the Yangtze-Huai River valley, the Korea Peninsula, and southern Japan. The connection in the lower-level pathway may be strengthened in the future.

Key words: CMIP6; global warming; South Asian monsoon; East Asian monsoon; future projection
CLC number: P467 **Document code:** A
Citation: CHEN Hong-jing, Song YANG, WEI Wei. Future Changes in the Relationship Between the South and East Asian Summer Monsoons in CMIP6 Models [J]. Journal of Tropical Meteorology, 2023, 29(2): 191-203, https://doi.org/10.46267/j.1006-8775.2023.015

1 INTRODUCTION

The South Asian summer monsoon (SASM) and the East Asian summer monsoon (EASM) are important components of the Asian monsoon (Tao and Chen [1]). Previous studies have investigated the relationships between the SASM and the EASM and demonstrated that summer rainfall in South Asia is positively correlated with that in northern China (Guo and Wang [2]; Kripalani and Singh [3]; Zhang [4]; Wu [5]; Greatbatch et al. [6]; Wu [7]) but negatively correlated with the rainfalls in the Yangtze River valley, southern Korea and southern Japan (Wu [5]; Krishnan and Sugi [8]).

Substantial efforts have been devoted to revealing the dynamic mechanisms for the relationships between the two monsoon components, and these mechanisms can generally be grouped into two plausible pathways. In the tropics, the water vapor transportation to East Asia from the western Pacific is negatively correlated with that from the SASM region. Intense western North Pacific subtropical high (WNPSH) with more water vapor along its southwestern flank to the Yangtze River Valley (YRV) is associated with weaker moisture flow in the SASM region, which leads to a negative relationship between the SASM rainfall and the YRV rainfall (Zhang [4, 9]; Li et al. [10]; Liu and Ding [11]). In the mid-latitudes, an upper-level zonal wave pattern, which is associated with the SASM rainfall and propagates eastward along the westerly jet stream, connects the SASM and the EASM (Wu [5]; Greatbatch et al. [6]; Krishnan and Sugi [8]; Lu et al. [12]; Kim et al. [13]; Ding and Wang [14]). More latent heat release associated with stronger SASM rainfall may trigger a wave pattern with anticyclonic anomalies over Central Asia and Northeast Asia and an anomalous cyclone over eastern China, which further influences the EASM rainfall (Wei et al. [15–16]). This wave pattern, representing the interaction between the SASM and the EASM, can be also reflected in the zonal shift of the South Asian high, which exerts a

Received 2022-10-11; **Revised** 2023-02-15; **Accepted** 2023-05-15
Funding: Guangdong Major Project of Basic and Applied Basic Research Foundation (2020B0301030004); National Natural Science Foundation of China (41975074); Guangdong Basic and Applied Basic Research Foundation (2023A1515010908); Guangdong Province Key Laboratory for Climate Change and Natural Disaster Studies (2020B1212060025); Innovation Group Project of Southern Marine Science and Engineering Guangdong Laboratory (Zhuhai) (311021001)
Biography: CHEN Hong-jing, M. S., primarily undertaking research on Asian monsoon.
Corresponding author: WEI Wei, e-mail: weiwei48@mail.sysu.edu.cn

dynamic effect on the zonal extension of the WNPSH (Wei et al. [17]). Thus, the teleconnection between the SASM and the EASM can be reflected in the zonal wave pattern in the mid-latitudes and the intensity of the WNPSH. Moreover, the relationship between the SASM and the EASM may be modulated by other factors such as the El Niño-Southern Oscillation (ENSO) (Hu et al. [18]; Ha et al. [19]; Lin et al. [20]), the Indian Ocean Dipole (Ha et al. [19]), and so on.

It should be noted that the relationship between the SASM and EASM rainfall variations is non-stationary, which has experienced a decadal decrease around the end of the 1970s (Wu [7]; Guo [21]; Wang and Huang [22]; Kripalani and Kulkarni [23]). Several possible factors contributing to the long-term changes in this relationship are suggested, including the changes in the mid-latitude wave pattern (Wu [5]; Wu [7]; Wang et al. [24]), the changes in the connection between anomalous SASM heating and mid-latitude circulation (Wang et al. [24]), ENSO (Wang and Huang [22]), and the zonal sea surface temperature (SST) gradient (Yun et al. [25]).

Under the global warming, the weakened SASM circulation (Ueda et al. [26]; Li et al. [27]) and the strengthened EASM circulation are projected (Li et al. [27]; Li et al. [28]) in the future, whereas both SASM and EASM rainfalls are projected to increase (Li et al. [27]; Wang et al. [29]; Ha et al. [30]; Chen et al. [31]; Wang et al. [32]). However, it is still unclear how the relationship between the SASM and the EASM will change under the global warming. The main purpose of this study is thus to investigate the future changes in the relationship between the SASM and the EASM.

The remainder of this paper is organized as follows. Section 2 is a description of the datasets and methods applied in this study. In section 3, we show the circulation features associated to the relationship between the SASM and the EASM in observations and CMIP6 models and evaluate the simulation skill of CMIP6 models in reproducing the connection between the SASM and the EASM. The future projections of the relationship between the two important monsoon components are discussed in section 4. Finally, conclusions and discussion are presented in section 5.

2 DATA AND METHODS

There are 26 coupled general circulation models (CGCMs) from the CMIP6 used in this study, including the historical runs from 1850 to 2014 and the SSP585 runs from 2015 to 2100 (Table 1). The historical runs are conducted under the changing conditions consistent with observations. The SSP585 runs are chosen as a high emission scenario in the CMIP6, assuming that radiative forcing will increase and then stabilize at about 8.5 W m^{-2} after 2100. Details of the CMIP6 models and experiments are available online (WGCM[33]) and in many previous studies (e. g. Eyring et al. [34]). Multi-model ensemble (MME) is used to reduce the uncertainties related to the CGCMs simulations / projections.

Table 1. Details of the CMIP6 models used in this study. The six models that meet the combined condition are selected to conduct the future projection analysis (denoted in bold).

Model	Institution	Resolution (lat. × lon.)
ACCESS-CM2	Commonwealth Scientific and Industrial Research Organization, Australian Research Council Centre of Excellence for Climate System, Australia	144×192
BCC-CSM2-MR	Beijing Climate Center, China	160×320
CAMS-CSM1-0	Chinese Academy of Meteorological Sciences, China	160×320
CanESM5	Canadian Centre for Climate Modeling and Analysis, Canada	64×128
CESM2	National Center for Atmospheric Research, USA	192×288
CESM2-WACCM		192×288
CMCC-ESM2	Fondazione Centro Euro-Mediterraneo sui Cambiamenti Climatici, Italy	192×288
CNRM-CM6-1	Centre National de Recherches Meteorologiques, Centre Europeen de Recherche et de Formation Avancee en Calcul Scientifique, France	128×256
CNRM-ESM2-1		128×256
EC-Earth3-Veg	EC-Earth Consortium, Europe	256×512
EC-Earth3		256×512
FGOALS-g3	Chinese Academy of Sciences, China	80×180
GFDL-CM4	National Oceanic and Atmospheric Administration, Geophysical Fluid Dynamics Laboratory, USA	90×144
HadGEM3-GC31-LL	Met Office Hadley Centre, UK	145×192

Model	Institution	Resolution (lat. × lon.)
INM-CM4-8	Institute of Numerical Mathematics of the Russian Academy of Science, Russia	120×180
INM-CM5-0		120×180
IPSL-CM6A-LR	Institute Pierre Simon Laplace, France	143×144
KACE-1-0-G	National Institute of Meteorological Sciences/Korea Meteorological Administration, Climate Research Division, Korea	145×192
MIROC-ES2L	Japan Agency for Marine-Earth Science and Technology, Atmosphere and Ocean Research Institute, National Institute for Environmental Studies, RIKEN Center for Computational Science, Japan	64×128
MIROC6		128×256
MPI-ESM1-2-HR	Max Planck Institute for Meteorology, Germany	192×384
MRI-ESM2-0	Meteorological Research Institute, Japan	160×320
NESM3	Nanjing University of Information Science and Technology, China	96×192
NorESM2	NorESM Climate Modeling Consortium, Norway	96×144
TaiESM1	Research Center for Environmental Changes, China	192×288
UKESM1-0-LL	Met Office Hadley Centre, UK	145×192

The observation data used for the period 1979–2014 are as follows: 1) the European Centre for Medium-range Weather Forecasts fifth major global reanalysis (ERA5) with a 1° × 1° resolution (Hersbach et al. [35]) for geopotential height and winds; 2) the Global Precipitation Climatology Project (GPCP) data version 2.2 with a 2.5° × 2.5° resolution for precipitation (Adler et al. [36]); 3) the All-India Rainfall Index (AIRI) from the Indian Institute of Tropical Meteorology (IITM [37]; Parthasarathy et al. [38]); 4) the Hadley Centre Sea Ice and Sea Surface Temperature dataset with a 1° × 1° resolution (HadISST; Rayner et al. [39]).

A 36-yr period is applied to the analysis of both the present climate from 1979 to 2014 and the future climate from 2064 to 2099. We calculate the summer mean values using the monthly data from June to August (JJA). To validate the performance of the CMIP6 models in their historical simulations with respect to observations, both observation data and model output are interpolated to the resolution of 2.5° × 2.5° using a bilinear interpolation method. To focus on the changes in the teleconnection between the SASM and the EASM, the zonal mean component is removed from the geopotential height.

In the regression analysis, a significance test for observations and individual models is carried out by using the Student's *t*-test. Following Chen and Yu [40], multi-model ensemble (MME) anomalies are significant at the 95% confidence level if

$$\left| Var_{\mathrm{MME}} \right| \geqslant \frac{\mathrm{STDDEV} \times \lambda}{\sqrt{N}}$$

where $|Var_{\mathrm{MME}}|$ is the absolute value of the MME anomalies obtained from the regression analysis, and STDDEV represents the inter-model standard deviation. N is the number of models, and λ is 1.96. The values of MME shown in figures will be dotted only if they are significant at the 95% confidence level and more than 70% CMIP6 models show the same signs of the MME.

3 SIMULATION PERFORMANCE OF CMIP6 MODELS IN HISTORICAL RUNS

Figure 1a shows the regression of summer rainfall onto the AIRI in observation. Positive anomalies appear over northern China and negative anomalies are observed over western East Asia, the Yellow Sea, the East China Sea and southern Korea (Fig. 1a). The correlation between the AIRI and northern China rainfall averaged over 32.5°–40°N/105°–120°E (the dash line box in Fig. 1) is 0.31 for the 36 years, significant at the 90% confidence level according to the Student's *t*-test. Fig. 1b shows the CMIP6 MME of the regressed summer rainfall against the SASM rainfall in 7.5°–32.5°N / 70° – 85° E (the solid line box in Fig. 1b) in the historical run from 1979 to 2014. The rainfall over the west coast of India accounts for a major part of the total summer rainfall in SASM rainfall. Similar to observations (Fig. 1a), the MME shows the positive anomalies over northern China and negative anomalies over the Meiyu-Baiu regions (Fig. 1b). Also, some biases exist in CMIP6 models compared to observations (Fig. 1a). The MME underestimates the negative anomalies over the Meiyu-Baiu regions and fails in reproducing the positive anomalies over the north of the Indochina Peninsula (Fig. 1b).

The atmospheric circulation pattern associated with the SASM rainfall anomaly is shown in Fig. 2. At 200 hPa (Fig. 2a), corresponding to more rainfall in the SASM region, anomalous anticyclones are observed over southern Central Asia (hereafter SCAAC) and

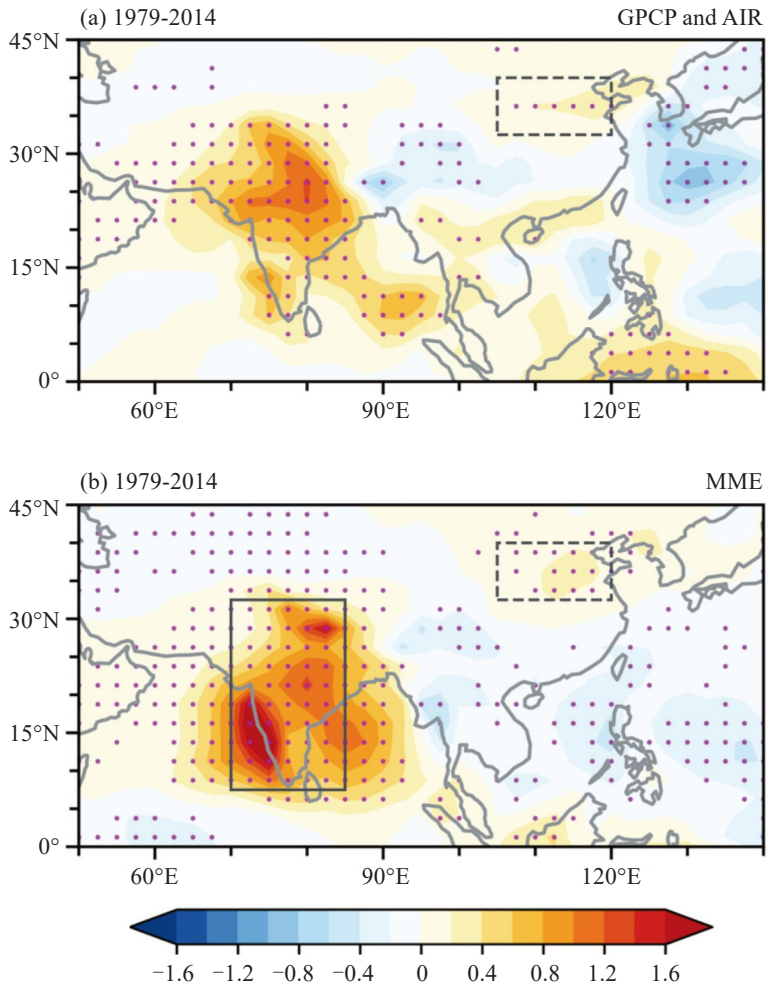

Figure 1. (a) Regression of the GPCP summer rainfall (mm day^{-1}) on the All-India Rainfall Index from 1979 to 2014. (b) CMIP6 MME of the regressed summer rainfall (mm day^{-1}) against the SASM rainfall in 7.5°−32.5°N/70°−85°E (the solid line box) in the historical run from 1979 to 2014. The stippled areas in (a) denote the regression coefficients that are significant at the 90% confidence level according to the Student's *t*-test, (b) denote that more than 70% CMIP6 models show the same signs of the MME and the MME mean is significant at the 95% confidence level. The dash line box represents the domain for calculating the area-mean northern China rainfall (32.5°−40°N, 105°−120°E).

Northeast Asia (hereafter NEAAC), while an anomalous cyclone is located to the north of the Indochina Peninsula. The SCAAC can be considered as a Rossby wave response to the diabatic heating in the SASM region. It propagates eastward along the mid-latitude westerly jet stream to Northeast Asia forming the NEAAC and influences the downstream areas (Wu [5]; Lu et al. [12]; Ding and Wang [14]). The NEAAC and the southward-located cyclonic anomaly can also be influenced by the negative latent heat anomaly released in association with anomalous rainfall over the EASM region (Wei et al. [16]). This mid-latitude wave pattern denotes the upper-level atmospheric response to the diabatic heating in the SASM and EASM regions and acts as the upper-level pathway in bridging the SASM and the EASM. At 500 hPa (Fig. 2c), the distribution of anomalous anticyclones in the mid-latitudes is similar to that at 200 hPa. In the tropics, a strengthened monsoon trough is observed over the Indian Peninsula and anomalous cyclonic anomalies appear over the northern Indochina Peninsula. At the lower troposphere (Fig. 2e), the strengthened Somali Jet and monsoon trough indicate a stronger SASM circulation. Besides, there is an anomalous anticyclone over the western North Pacific (hereafter WNPAC). The southerly anomalies carrying water vapor along the western edge of the WNPAC converge over northern China and thus lead to more rainfall in that region, while the northerly anomalies at the eastern edge of the WNPAC with less water vapor flow occur in southern Japan and thus lead to less rainfall there. The Meiyu-Baiu region is controlled by positive geopotential height anomalies, which is unfavorable for ascending motion and suppresses the rainfall in situ. These results are dynamically consistent to the positive and negative anomalies over northern China and southern Japan in Fig. 1a, respectively. The anomalous water vapor transportation along the western edge of the WNPAC

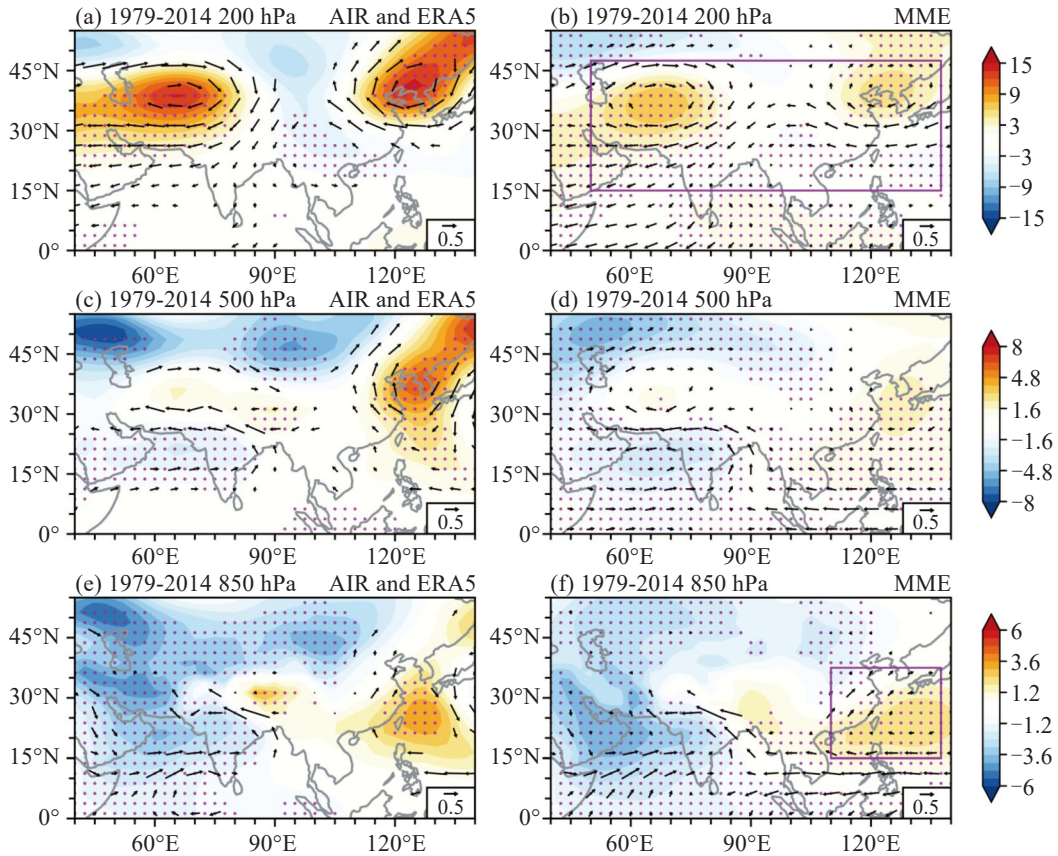

Figure 2. Regressions of the geopotential height (shading, units: gpm) and winds (vector, units: m s^{-1}) on the All-India Rainfall Index from 1979 to 2014, which are calculated at (a) 200 hPa, (c) 500 hPa and (e) 850 hPa, respectively. The CMIP6 MME of the regressed geopotential height (shading, units: gpm) and winds (vector, units: m s^{-1}) on the SASM rainfall index in the historical run from 1979 to 2014 is calculated at (b) 200 hPa, (d) 500 hPa, and (f) 850 hPa, respectively. The stippled areas and the black vectors in (a, c, e) denote that the regression coefficients are significant at the 95% confidence level according to the Student's *t*-test, (b, d, f) denote that more than 70% CMIP6 models show the same signs of the MME and the MME is significant at the 95% confidence level. The purple solid line boxes in (b) and (f) show the domain for calculating the pattern correlation coefficients at 200 hPa and 850 hPa, respectively.

related to the SASM rainfall denotes the lower-level pathway connecting the SASM and the EASM. In short, the EASM is connected to the SASM through the above-mentioned pathways, i.e. the mid-latitude wave pattern at the upper level and the anomalous water vapor transportation associated the WNPAC.

The right column of Fig. 2 shows the MME calculated by CMIP6 models in the historical run. It is shown that the CMIP6 models are capable of simulating the SCAAC and NEAAC at the upper level (Fig. 2b), the anomalous anticyclone over the southern Central Asia and monsoon trough at the middle level (Fig. 2d), and the WNPAC at the lower level (Fig. 2f), although the CMIP6 MME underestimates the SCAAC and the NEAAC. It should also be noted that the MME fails in reproducing the northerly anomalies over southern Japan due to the eastward deflection of the eastern edge of the WNPAC, which is consistent with the underestimation of the negative anomalies over southern Japan in Fig. 1b. In short, the CMIP6 MME is substantially capable of reproducing the upper-level wave pattern and water vapor transportation anomalies along the western edge of the WNPAC at the lower level, which means that the MME is able to reproduce the relationship between the SASM and the EASM.

To evaluate individual models' performance on simulating the relationship between the SASM and the EASM, we calculate the pattern correlation coefficient (PCC) between the observed and model-simulated geopotential height anomalies related to the SASM rainfall over 15° − 47.5° N / 50° − 137.5° E at 200 hPa (shown by the purple solid line box in Fig. 2b) for the upper-level pathway and 15° − 37.5° N / 110° − 137.5° E at 850 hPa (shown by the purple solid line box in Fig. 2f) for the lower-level pathway since these two pathways are the two key components related to the SASM-EASM teleconnection. The individual models' PCC ranges from −0.42 to 0.91 for the results calculated at the upper level (shown by the red numbers in Fig. 3) and ranges from −0.90 to 0.94 for the results calculated at the lower level (shown by the blue numbers in Fig. 3), which indicates significant inter-model spreads when

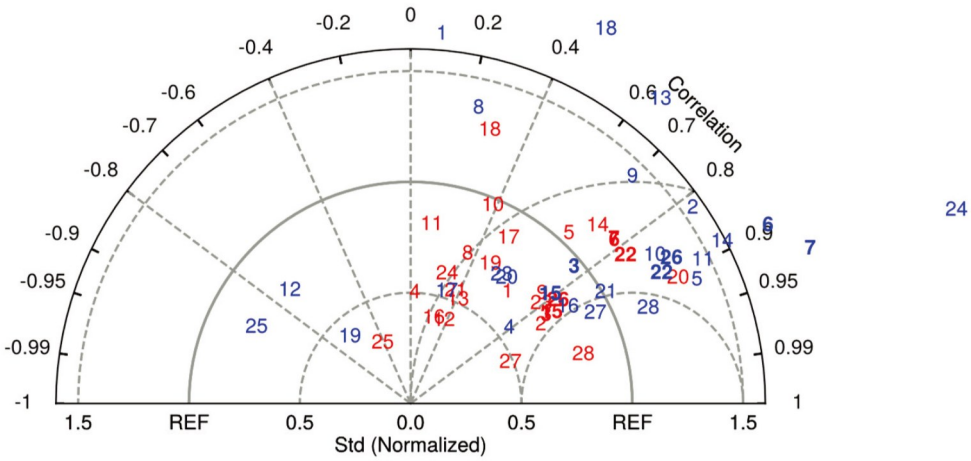

1 ACCESS-CM2	11 EC-Earth3-Veg	20 MIROC-ES2L
2 BCC-CSM2-MR	12 FGOALS-g3	21 MPI-ESM1-2-HR
3 CAMS – CSM1 – 0	13 GFDL-CM4	**22 MRI – ESM2 – 0**
4 CanESM5	14 HadGEM3-GC31-LL	23 NESM3
5 CESM2	**15 INM – CM4 – 8**	24 NorESM2-LM
6 CESM2 – WACCM	16 INM-CM5-0	25 TaiESM1
7 CMCC – ESM2	17 IPSL-CM6A-LR	**26 UKESM1 – 0 – LL**
8 CNRM-CM6-1	18 KACE-1-0-G	27 MME
9 CNRM-ESM2-1	19 MIROC6	28 gMME
10 EC-Earth3		

Figure 3. Taylor diagram of the pattern correlation coefficients between ERA5 reanalysis data and 26 CMIP6 models in the purple boxes presented in Fig. 2. The red and blue numbers are for the pattern correlation coefficients calculated at 200 hPa and 850 hPa, respectively. The numbers denoting the selected good models are shown in bold.

simulating the upper-level wave pattern and the lower-level WNPAC in the CMIP6 models. Especially, the upper-level MME has worse performance compared to individual models. Thus, the models that have better simulation skill in reproducing the connection between the SASM and the EASM should be chosen for the sake of more reliable MME construction and future projection.

Selection of the models is based on the correlation between the rainfall in the SASM and that in northern China and the upper- and lower-level PCCs. The models that satisfy that 1) the correlation between the rainfall in the SASM (averaged over 7.5°–32.5°N/70°–85°E) and that in northern China (averaged over 32.5°–40° N/105°–120° E) is positive and 2) the upper - and lower-level PCCs are over 0.75 are chosen. Six models are selected, which include CAMS-CSM1-0, CESM2-WACCM, CMCC-ESM2, INM-CM4-8, MRI-ESM2-0, and UKESM1-0-LL (denoted in bold in Table 1). Although the definition of combined skill and threshold value for the model selection are rather subjective, the advantages using the six good models' MME (hereafter gMME) are that 1) it has better simulation skills for the upper-level wave pattern and the lower-level WNPAC, which are the two pathways connecting the SASM and the EASM (Fig. 3) and 2) it contains less inter-model spreads compared to all the models' MME.

4 FUTURE CHANGES IN THE RELATIONSHIP BETWEEN THE SASM AND THE EASM

Figure 4a shows the gMME of the regressed summer rainfall onto the SASM rainfall index during 1979–2014. It is found that the gMME can reproduce the positive anomalies over northern China and the negative anomalies over the Meiyu-Baiu region, although the underestimation over the Yellow Sea, the East China Sea and the north of the Indochina Peninsula still exists (Fig. 4a). The first column in Fig. 5 shows the gMME of the regressed circulation anomalies onto the SASM rainfall index during 1979–2014. Compared to that in the MME (Fig. 2b, 2d and 2f), the upper-level wave pattern and the wind anomalies along the western and eastern edges of the WNPAC in gMME (Fig. 5a and 5g) are more similar to those in the observation. This may be attributed to the more rainfall simulated over the northern Indian Peninsula in the gMME, which plays a key role in maintaining the upper-level wave pattern (Wu [5]; Ding and Wang [14]; Wei et al. [15–16]).

In the future projections, the positive rainfall anomalies associated with SASM rainfall extend southward from northern China to the Yangtze-Huai River valley, the Korea Peninsula, and southern Japan (Fig. 4b). The positive relationship between the SASM rainfall and the rainfall over northern China is weakened

(Fig. 4c). The relationship between the SASM rainfall and the rainfall over the Korea Peninsula and southern Japan turns from negative to positive (Fig. 4b and 4c). Moreover, the positive rainfall anomalies are weaker over the northern Indian Peninsula and stronger over the southern Indian Peninsula in future (Fig. 4c). Besides, the upper-level divergence, ascending motions and the lower-level convergence over the northern Indian Peninsula tend to be weakened in the future scenario (Fig. 6b, 6d and 6f), consistent to the negative anomalies over northern South Asia in Fig. 4c.

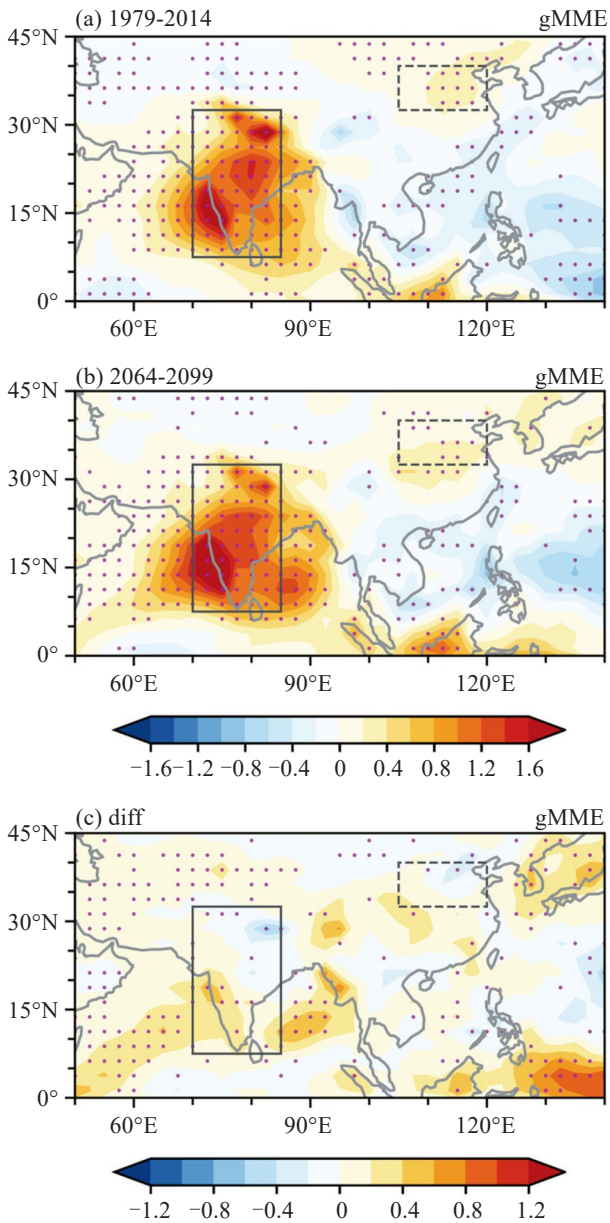

Figure 4. Same variables as Fig.1, but based on the 6 selected models in CMIP6 for periods (a) 1979−2014 and (b) 2064−2099. (c) shows the difference between (b) and (a). The purple dots in (c) represent the area where more than 70% of the selected models show the same signs of the gMME.

The second column of Fig. 5 shows the projected circulation anomalies in the future. At the upper level, the climatological westerly jet stream is predicted to become weaker in JJA, with its exit region moving westward (Fig. 5c). Furthermore, it is predicted that the SCAAC will shift northward while the NEAAC will shift southward, and both of them will become weaker in the future (Fig. 5b). These features are quite clear in the difference between the future scenario and the historical scenario (Fig. 5c). The weakened rainfall anomalies over northern South Asia may induce a cyclonic anomaly due to the Rossby wave response on its northwestern side and thus contribute to the northward movement of the SCAAC (Wei et al. [41]).

The weakened SCAAC and NEAAC imply a weakened upper-level wave pattern in the future.

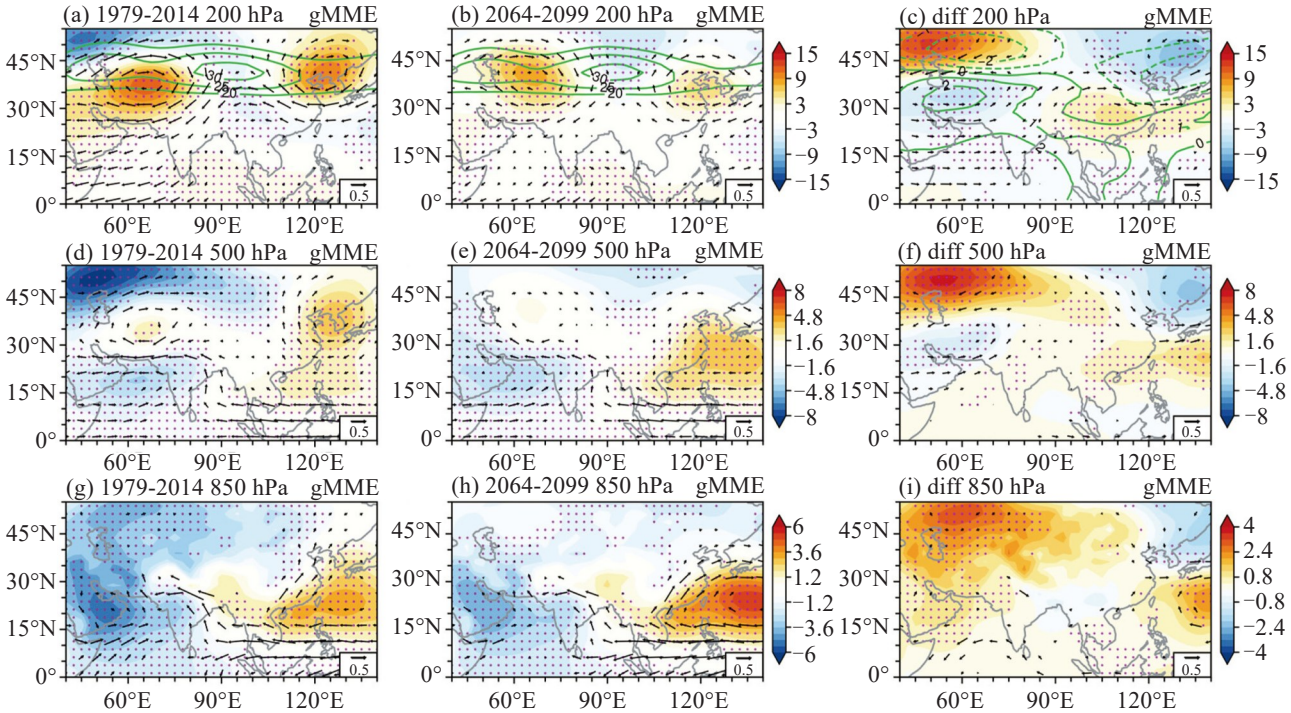

Figure 5. Same variables as Fig. 2, but based on the 6 selected models in CMIP6 for periods (a, d, g) 1979−2014 and (b, e, h) 2064−2099. (c, f, i) show the difference between the two periods respectively at different levels. The purple dots in (c, f , i) represent the area where more than 70% of the selected models show the same signs of gMME. The green contours in (a, b) denote the JJA zonal wind climatology at 200 hPa with levels 20, 25, and 30 m s^{-1} for periods (a) 1979−2014 and (b) 2064−2099 while those in (c) denote the difference in JJA zonal wind climatology at 200 hPa between 2064−2099 and 1979−2014 with levels −2, −1, 0, 1, and 2 m s^{-1}.

According to previous studies, this upper-level wave pattern in the mid-latitudes is tightly connected to the anomalous condensational latent heat over the northern Indian Peninsula (Greatbatch et al. [6]; Wei et al. [15−16]) and propagates along the mid-latitude westerly jet stream, influencing the downstream areas (Wu [5]; Lu et al. [12]; Ding and Wang [14]). Therefore, the weakening rainfall anomalies over northern South Asia may contribute to the weakening of the SCAAC and further lead to the weakened NEAAC in the downstream region. On the other hand, the westward shift of the westerly jet exit may be unfavorable to the Rossby wave energy dispersion along the mid-latitude westerly jet stream, which may contribute to the weakening of the NEAAC.

With the weakened and southward shifted NEAAC, the upper-level divergence anomalies are weakened and shift southward from northern China to the Yangtze-Huai River valley. The convergence over the eastern Meiyu-Baiu region is weakened (Fig. 6b). Accordingly, the ascending motions over northern China tend to be weakened and shift southward to the Yangtze-Huai River valley, while the descending motions over the eastern Meiyu-Baiu region are weakened at the middle troposphere (Fig. 6d). The weakening and southward shifting upper-level divergence and ascending motions are in favor of the southward shift of rainfall from northern China to the Yangtze-Huai River valley. In short, the weakening SCAAC and NEAAC, indicating the weakening upper-level teleconnection between the SASM and the EASM in the mid-latitudes, are dynamically consistent with the weakening relationship between the precipitation anomalies over northern China and the SASM rainfall.

At the lower level, the WNPAC is projected to become stronger in the future, with stronger southerlies along its western edge (Fig. 5h). The anomalous southerlies carrying water vapor converge at 35 ° N. These results are consistent to the southward shift of the positive rainfall anomalies from northern China to the Yangtze-Huai River valley and the eastern Meiyu-Baiu region.

We also investigate the long-term changes in the SCAAC, the NEAAC and the WNPAC in individual models (Fig. 7). It can be seen that all of the 26 CMIP6 models can reproduce the SCAAC in the historical runs although two of them are very weak. 17 (65.4%) models project that the SCAAC will become weaker while eight models simulate that it will strengthen (Fig. 7a) in the future. Five (83.3%) of the selected models consider that the SCAAC will become weaker in the future scenario. Among the 23 models that can properly simulate the negative vorticity anomalies of the NEAAC, 13 (56.5%) models project that the NEAAC will weaken in the future (Fig. 7b). One model considers that the NEAAC will change into an anomalous cyclone. Nine (39.1%) models project that the NEAAC will strengthen. While

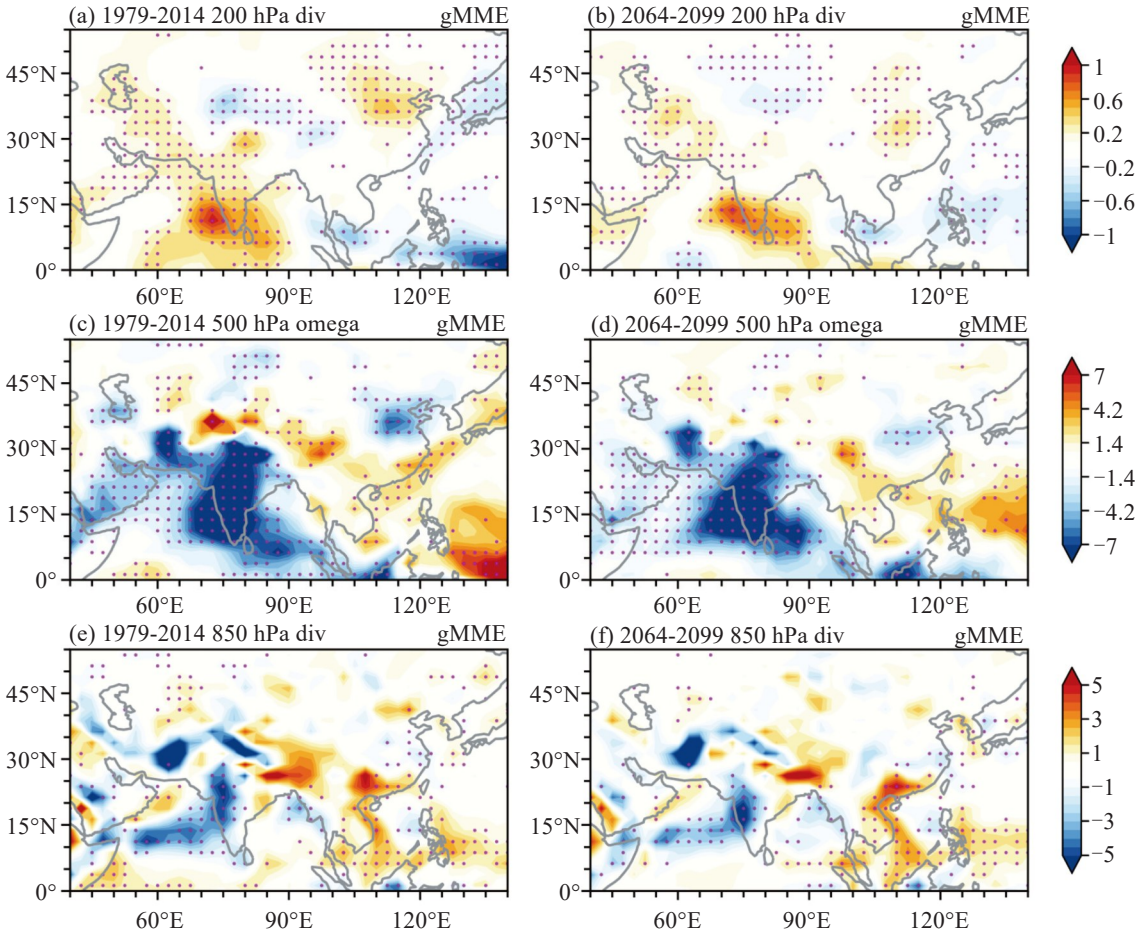

Figure 6. CMIP6 gMME of regressed (a, b) 200-hPa (units: 10^{-6} s^{-1}) and (e, f) 850-hPa divergence (units: 10^{-7} s^{-1}) and (c, d) 500-hPa vertical velocity (units: 10^{-3} Pa s^{-1}) against the SASM rainfall index in the historical run from 1979 to 2014 (left column) and in the SSP585 run from 2064 to 2099 (right column). The stippled areas denote that more than 70% of the selected models show the same signs of the gMME and the gMME is significant at the 95% confidence level.

considering the selected models, the uncertainty of projection decreases. Five (83.3%) of the six selected models project that the NEAAC will weaken in the future. In the historical scenario, 23 models can simulate the WNPAC (Fig. 7c). 15 (62.5%) of them consider that the WNPAC will strengthen in the future and 7 (29.1%) of them consider that it will weaken. Four (66.7%) of the selected models simulate that it will strengthen in the future. In summary, most of the 26 CMIP6 models can properly simulate the anomalous circulation features related to the SASM rainfall. Among these models, over half of them simulate that the SCAAC and the NEAAC tend to be weakened and the WNPAC will strengthen in the future. The future projections of the SCAAC exhibit a relatively small inter-model spread compared to those of the NEAAC and the WNPAC. When considering the six selected models, the results are the same and have smaller inter-model spread. Therefore, not only the gMME but also more than half of the CMIP6 models show that the SCAAC and the NEAAC will weaken but the WNPAC will strengthen.

Previous studies have shown the importance of SST on modulating the relationship between the SASM and the EASM (Ha et al. [19]; Lin et al. [20]). Considering that the SST is projected to change under the global warming, it is necessary to investigate the role of the changing SST in modulating the relationship between the SASM and the EASM. Fig. 8 shows the SST anomalies obtained by regression with respect to the SASM rainfall. In observation (Fig. 8a), the negative SST anomalies over the eastern equatorial Pacific indicate a La Niña-like pattern corresponding to more SASM rainfall. The enhanced vertical motions over the Maritime Continent associated with the La Niña-like pattern strengthen the WNPAC by modulating the local Hadley circulation (Chung et al. [42]). Besides, the positive anomalies over the Yellow Sea, northeast coast of Japan, and the North Pacific are connected to the anomalous sinking motions (Fig. 6c), and the negative rainfall anomalies in situ can be considered as a response to the circulation anomalies. Thus, the SST anomalies in the eastern equatorial Pacific are the key factor in modulating the observational relationship between the SASM and the EASM.

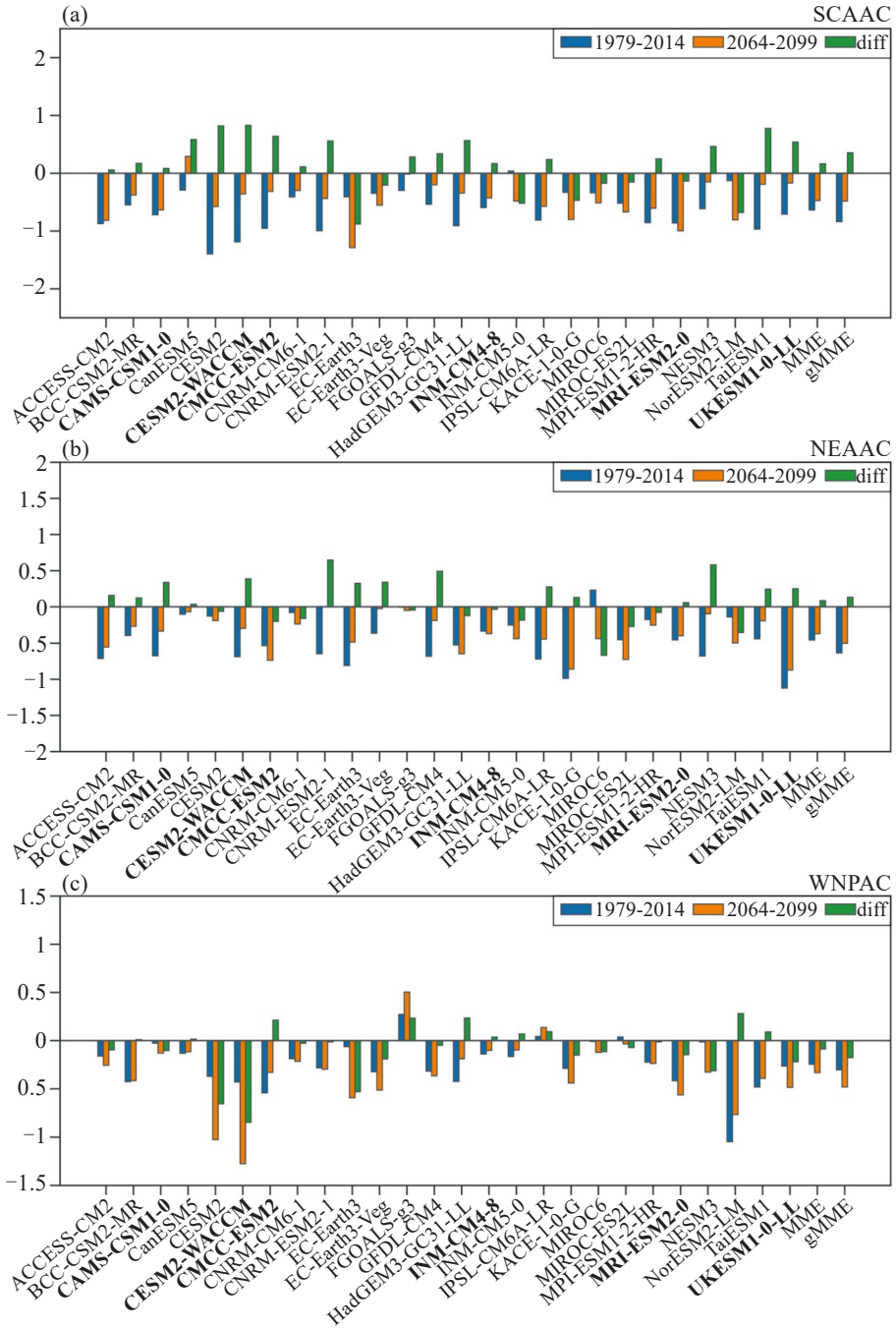

Figure 7. Anomalies of area-mean vorticity (units: 10^{-6} s^{-1}) obtained by regressing on the area-mean SASM rainfall of CMIP6 models for periods 1979−2014 (blue) and 2064−2099 (orange), and the difference between 2064−2099 and 1979−2014 (green). (a) is for southern Central Asia (25°−50°N/50°−80 °E), (b) for Northeast Asia (27.5°−50.0°N/105.0°−137.5 °E), and (c) for western North Pacific (15.0°−37.5 °N/110.0°−137.5 °E).

The gMME overestimates the SST over the Maritime Continent, the North Pacific and the range of negative SST anomalies in the equatorial Pacific Ocean (Fig. 8b). Consistent with the overestimation of the range of negative SST anomalies in the equatorial Pacific Ocean, the ascending motions over the Maritime Continent and sinking motions over the equatorial western Pacific shift westward (Fig. 8b) compared to the observation (Fig. 8a). Overall, the selected models can simulate the distribution of SST and vertical motion anomalies related to the SASM rainfall (Fig. 8b).

Models project that the negative SST anomalies over the eastern equatorial Pacific become weaker in the future, which is consistent with the weaker sinking motions over the western equatorial Pacific due to the weaker Walker circulation. According to Lin et al. [20], the rainfall over the SASM and northern China tend to increase/decrease synchronously under La Niña/El Niño condition with cooler/warmer SST over the central and eastern equatorial Pacific in the concurrent summer.

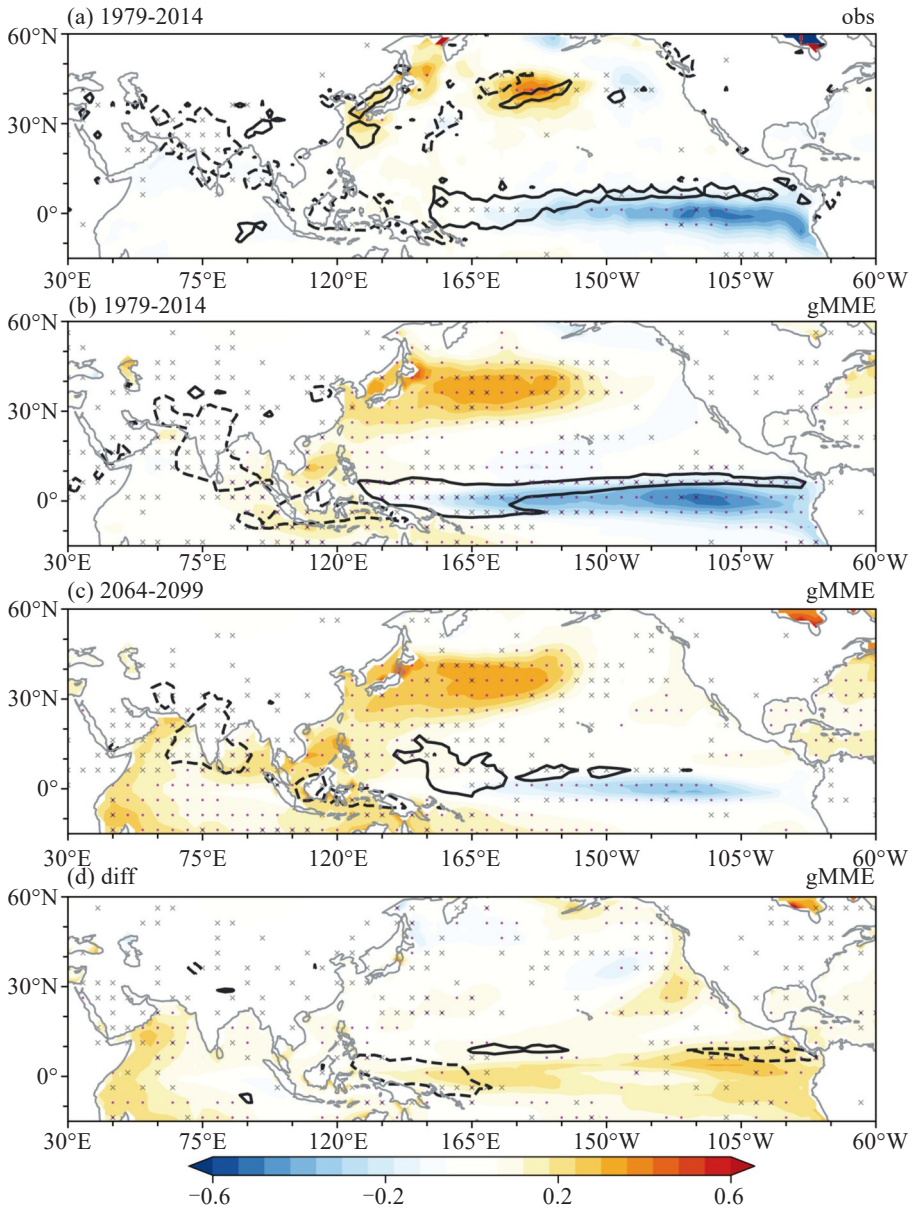

Figure 8. (a) Regression of the summer HadISST (shading, units: K) and vertical velocity (shading, units: Pa s^{-1}) on the All-India Rainfall Index from 1979 to 2014. CMIP6 gMME of the regressed summer SST (shading, units: K) and vertical velocity (shading, units: Pa s^{-1}) against the area-mean SASM rainfall is calculated in (b) the historical run from 1979 to 2014 and (c) the SSP585 run from 2064 to 2099. (d) shows the difference between 2064−2099 and 1979−2014. For the vertical velocity anomalies, the solid (dashed) contour lines denote positive (negative) values with levels 0.005 and −0.005 Pa s^{-1}. The purple dots (grey crosses) in (a) denote the significant regression coefficients of SST (vertical velocity) above the 95% confidence level according to the Student's *t*-test, (b, c) more than 70% of the selected models show the same signs of SST (vertical velocity) of gMME and the multi-model ensemble mean is significant at the 95% confidence level.

Therefore, the decrease in negative SST anomalies over the eastern equatorial Pacific in the future may contribute to the weakening relationship between the SASM rainfall and the northern China rainfall. However, it should be noted that the changes in SST anomalies (Fig. 8d) are similar to the long-term trends under the global warming (Ruela et al. [43]). The SST anomalies associated to the SASM rainfall show no significant change after removing the long-term trends (figure not shown). Therefore, the role of background SST anomalies in modulating the relationship between the SASM and the EASM under the global warming needs further investigations.

According to Lin et al. [44], the relationship between the SASM and the EASM has been focused mainly on interannual timescale. We also remove the long-term linear trends in the period of 1979−2099 to focus on the year-to-year variations. The results (figures not shown) about precipitation anomalies and circulation anomalies exhibit no significant changes compared to the non-detrended results, which means that the weakened mid-latitude wave pattern, the strengthened WNPAC and the

weakened relationship between the SASM and the EASM rainfall still exist without the long-term trends.

5 CONCLUSIONS AND DISCUSSION

In this study, we have examined the capabilities of global climate models in simulating the relationship between the SASM and the EASM and further explored the future changes in this relationship. The SASM and the EASM are connected through a mid-latitude upper-level wave pattern and the water vapor transportation anomalies along the western edge of the western North Pacific subtropical high. The MME of CMIP6 models can capture the relationship between the SASM and the EASM, but underestimate the upper-level circulation anomalies. To improve the simulation skills and decrease the inter-model uncertainties, six models are selected based on their upper- and lower-level PCCs in reproducing the teleconnection at the upper level and the water vapor transportation along the WNPAC at the lower level. In the future projection, the upper-level wave pattern in the mid-latitudes tends to be weakened, which may be contributed by the decreased rainfall anomalies over northern Indian Peninsula. At the lower level, the WNPAC is projected to strengthen with stronger water vapor transportation along its western edge. Besides, the negative SST anomalies over the eastern equatorial Pacific may be weakened in the future. Corresponding to these features, the positive (negative) rainfall anomalies associated with positive (negative) SASM rainfall anomalies are projected to extend southward from northern China to the Yangtze-Huai River valley, the Korea Peninsula, and southern Japan. Thus, the connection in the lower-level pathway may be strengthened in the future.

REFERENCES

[1] TAO S Y, CHEN L X. A review of recent research on the East Asian summer monsoon in China [M]// CHANG C P, KRISHNAMURTI T N (eds), Monsoon Meteorology. New York: Oxford University Press, 1987: 60-92.

[2] GUO Q Y, WANG J Q. A comparative study on summer monsoon in China and India [J]. Journal of Tropical Meteorology, 1988, 4(1): 53-60 (in Chinese).

[3] KRIPALANI R H, SINGH S V. Large scale aspects of India-China summer monsoon rainfall [J]. Advances in Atmospheric Sciences, 1993, 10(1): 71-84, https://doi.org/10.1007/BF02656955

[4] ZHANG R H. The role of Indian summer monsoon water vapor transportation on the summer rainfall anomalies in the northern part of China during the El Niño mature phase [J]. Plateau Meteor, 1999, 18(4): 567-574 (in Chinese).

[5] WU R G. A mid-latitude Asian circulation anomaly pattern in boreal summer and its connection with the Indian and East Asian summer monsoons [J]. International Journal of Climatology, 2002, 22(15): 1879-1895, https://doi. org / 10.1002/joc.845

[6] GREATBATCH R J, SUN X G, YANG X Q. Impact of variability in the Indian summer monsoon on the East Asian summer monsoon [J]. Atmospheric Science Letters, 2013, 14(1): 14-19, https://doi.org/10.1002/asl2.408

[7] WU R G. Relationship between Indian and East Asian summer rainfall variations [J]. Advances in Atmospheric Sciences, 2017, 34(1): 4-15, https://doi. org / 10.1007 / s00376-016-6216-6

[8] KRISHNAN R, SUGI M. Baiu rainfall variability and associated monsoon teleconnections [J]. Journal of the Meteorological Society of Japan, 2001, 79(3): 851-860, https://doi.org/10.2151/jmsj.79.851

[9] ZHANG R H. Relations of water vapor transport from Indian monsoon with that over East Asia and the summer rainfall in China [J]. Advances in Atmospheric Sciences, 2001, 18(5): 1005-1017, https://doi. org / 10.1007 / BF03403519

[10] LI X F, JIANG Z H, SHI Y. Moisture transport paths and sources of South China annually first rainy season and their relationship with the onset of the South China Sea summer monsoon [J]. Journal of Tropical Meteorology, 2019, 25(2): 171-179, https://doi. org / 10.16555 / j. 1006-8775.2019.02.004

[11] LIU Y Y, DING Y H. Analysis and numerical simulation of the teleconnection between Indian summer monsoon and precipitation in North China [J]. Acta Meteorologica Sinica, 2008, 66(5): 789-799 (in Chinese), https://doi.org/10.11676/qxxb2008.072

[12] LU R Y, OH J H, KIM B J. A teleconnection pattern in upper-level meridional wind over the North African and Eurasian continent in summer [J]. Tellus A: Dynamic Meteorology and Oceanography, 2002, 54(1): 44-55, https://doi.org/10.3402/tellusa.v54i1.12122

[13] KIM B J, MOON S E, LU R Y, et al. Teleconnections: summer monsoon over Korea and India [J]. Advances in Atmospheric Sciences, 2002, 19(4): 665-676, https://doi.org/10.1007/s00376-002-0006-z

[14] DING Q H, WANG B. Circumglobal teleconnection in the Northern Hemisphere summer [J]. Journal of Climate, 2005, 18(17): 3483-3505, https://doi. org / 10.1175 / JCLI3473.1

[15] WEI W, ZHANG R H, WEN M, et al. Impact of Indian summer monsoon on the South Asian High and its influence on summer rainfall over China [J]. Climate Dynamics, 2014, 43(5-6): 1257-1269, https://doi. org / 10.1007/s00382-013-1938-y

[16] WEI W, ZHANG R H, WEN M, et al. Interannual variation of the South Asian High and its relation with Indian and East Asian summer monsoon rainfall [J]. Journal of Climate, 2015, 28(7): 2623-2634, https://doi.org/10.1175/JCLI-D-14-00454.1

[17] WEI W, ZHANG R H, WEN M, et al. Dynamic effect of the South Asian high on the interannual zonal extension of the western North Pacific subtropical high [J]. International Journal of Climatology, 2019, 39(14): 5367-5379, https://doi.org/10.1002/joc.6160

[18] HU Z Z, WU R G, KINTER III J L, et al. Connection of summer rainfall variations in South and East Asia: role of El Niño-southern oscillation [J]. International Journal of Climatology, 2005, 25(9): 1279-1289, https://doi. org / 10.1002/joc.1159

[19] HA K J, SEO Y W, LEE J Y, et al. Linkages between the South and East Asian summer monsoons: a review and revisit [J]. Climate Dynamics, 2018, 51(11-12): 4207-4227, https://doi.org/10.1007/s00382-017-3773-z

[20] LIN D W, BUEH C, XIE Z W. A study on the coupling relationships among the Pacific sea surface temperature and summer rainfalls over North China and India [J]. Chinese Journal of Atmospheric Sciences, 2018, 42(6): 1175-1190 (in Chinese), https://doi. org / 10.3878 / j. issn.1006-9895.1712.17183

[21] GUO Q Y. Teleconnection between the floods/droughts in North China and Indian summer monsoon rainfall [J]. Acta Geographica Sinica, 1992, 47(5): 394-402 (in Chinese), https://doi.org/10.11821/xb199205002

[22] WANG S W, HUANG J B. Instability of precipitation teleconnection between North China and India [J]. Progress in Natural Science, 2006, 16(8): 980-985 (in Chinese).

[23] KRIPALANI R H, KULKARNI A. Monsoon rainfall variations and teleconnections over South and East Asia [J]. International Journal of Climatology, 2001, 21(5): 603-616, https://doi.org/10.1002/joc.625

[24] WANG H, WANG B, HUANG F, et al. Interdecadal change of the boreal summer circumglobal teleconnection (1958-2010) [J]. Geophysical Research Letters, 2012, 39 (12): L12704, https://doi.org/10.1029/2012GL052371

[25] YUN K S, LEE J Y, HA K J. Recent intensification of the South and East Asian monsoon contrast associated with an increase in the zonal tropical SST gradient [J]. Journal of Geophysical Research: Atmospheres, 2014, 119(13): 8104-8116, https://doi.org/10.1002/2014JD021692

[26] UEDA H, IWAI A, KUWAKO K, et al. Impact of anthropogenic forcing on the Asian summer monsoon as simulated by eight GCMs [J]. Geophysical Research Letters, 2006, 33(6): L06703, https://doi. org / 10.1029 / 2005GL025336

[27] LI T, WANG Y H, WANG B, et al. Distinctive South and East Asian monsoon circulation responses to global warming [J]. Science Bulletin, 2022, 67(7): 762-770, https://doi.org/10.1016/j.scib.2021.12.001

[28] LI Z B, SUN Y, LI T, et al. Future changes in East Asian summer monsoon circulation and precipitation under 1.5 to 5 °C of warming [J]. Earth's Future, 2019, 7(12): 1391-1406, https://doi.org/10.1029/2019EF001276

[29] WANG B, YIM S Y, LEE J Y, et al. Future change of Asian-Australian monsoon under RCP 4.5 anthropogenic warming scenario [J]. Climate Dynamics, 2014, 42(1-2): 83-100, https://doi.org/10.1007/s00382-013-1769-x

[30] HA K J, MOON S, TIMMERMANN A, et al. Future changes of summer monsoon characteristics and evaporative demand over Asia in CMIP6 simulations [J]. Geophysical Research Letters, 2020, 47(8): e2020GL087492, https://doi.org/10.1029/2020GL087492

[31] CHEN Z M, ZHOU T J, ZHANG L X, et al. Global land monsoon precipitation changes in CMIP6 projections [J]. Geophysical Research Letters, 2020, 47(14): e2019GL086902, https://doi.org/10.1029/2019GL086902

[32] WANG B, BIASUTTI M, BYRNE M P, et al. Monsoons climate change assessment [J]. Bulletin of the American Meteorological Society, 2021, 102(1): E1-E19, https://doi.org/10.1175/BAMS-D-19-0335.1

[33] WGCM. Coupled Model Intercomparison Project Phase 6 [EB/OL]. [2022-10-07]. https://pcmdi.llnl.gov/CMIP6/

[34] EYRING V, BONY S, MEEHL G A, et al. Overview of the Coupled Model Intercomparison Project Phase 6 (CMIP6) experimental design and organization [J]. Geoscientific Model Development, 2016, 9(5): 1937-1958, https://doi.org/10.5194/gmd-9-1937-2016

[35] HERSBACH H, BELL B, BERRISFORD P, et al. The ERA5 global reanalysis [J]. Quarterly Journal of the Royal Meteorological Society, 2020, 146(730): 1999-2049, https://doi.org/10.1002/qj.3803

[36] ADLER R F, HUFFMAN G J, CHANG A, et al. The version-2 Global Precipitation Climatology Project (GPCP) monthly precipitation analysis (1979-present) [J]. Journal of Hydrometeorology, 2003, 4(6): 1147-1167, https://doi. org / 10.1175 / 1525-7541(2003)004<1147: TVGPCP>2.0.CO;2

[37] IITM. Meteorological Data Sets for downloading [EB / OL]. [2022-10-07]. https://www. tropmet. res. in / Data% 20Archival-51-Page

[38] PARTHASARATHY B, MUNOT A A, KOTHAWALE D R. All-India monthly and seasonal rainfall series: 1871-1993 [J]. Theoretical and Applied Climatology, 1994, 49 (4): 217-224, https://doi.org/10.1007/BF00867461

[39] RAYNER N A, PARKER D E, HORTON E B, et al. Global analyses of sea surface temperature, sea ice, and night marine air temperature since the late nineteenth century [J]. Journal of Geophysical Research: Atmospheres, 2003, 108(D14): 4407, https://doi. org / 10.1029/2002JD002670

[40] CHEN S F, YU B. The seasonal footprinting mechanism in large ensemble simulations of the second generation Canadian earth system model: uncertainty due to internal climate variability [J]. Climate Dynamics, 2020, 55(9-10): 2523-2541, https://doi. org / 10.1007 / s00382-020-05396-y

[41] WEI W, ZHANG R H, YANG S, et al. Quasi-biweekly oscillation of the South Asian High and its role in connecting the Indian and East Asian summer rainfalls [J]. Geophysical Research Letters, 2019, 46(24): 14742-14750, https://doi.org/10.1029/2019GL086180

[42] CHUNG P H, SUI C H, LI T. Interannual relationships between the tropical sea surface temperature and summertime subtropical anticyclone over the western North Pacific [J]. Journal of Geophysical Research: Atmospheres, 2011, 116(D13): D13111, https://doi. org / 10.1029/2010JD015554

[43] RUELA R, SOUSA M C, DECASTRO M, et al. Global and regional evolution of sea surface temperature under climate change [J]. Global and Planetary Change, 2020, 190: 103190, https://doi. org / 10.1016 / j. gloplacha.2020.103190

[44] LIN D W, BUEH C, XIE Z W. Relationship between summer rainfall over North China and India and its genesis analysis [J]. Chinese Journal of Atmospheric Sciences, 2016, 40(1): 201-214 (in Chinese), https://doi. org/10.3878/j.issn.1006-9895.1503.14339

Citation: CHEN Hong-jing, Song YANG, WEI Wei. Future Changes in the Relationship Between the South and East Asian Summer Monsoons in CMIP6 Models [J]. Journal of Tropical Meteorology, 2023, 29(2): 191-203, https://doi.org/10.46267/j.1006-8775.2023.015